RSC Advances

ROYAL SOCIETY OF CHEMISTRY

www.rsc.org/advances

Role of Carbon Coating in Improving Electrochemical Performance of Li-rich $Li(Li_{0.2}Mn_{0.54}Ni_{0.13}Co_{0.13})O_2$ Cathode

Bohang Song,[a,†] *Cuifeng Zhou,*[b] *Yu Chen,*[c] *Zongwen Liu,*[b] *Man On Lai,*[a] *Junmin Xue,*[c] *Li Lu*[a,*]

[a] Materials Science Laboratory, Department of Mechanical Engineering, National University of Singapore, Singapore 117576.

[b] School of Chemical and Biomolecular Engineering, The University of Sydney, Sydney, Australia.

[c] Department of Materials Science and Engineering, National University of Singapore, Singapore 117576.

ABSTRACT:

Li-rich $Li(Li_{0.2}Mn_{0.54}Ni_{0.13}Co_{0.13})O_2$ cathode coated with carbon layer has been prepared by a hydrothermal approach followed by a post annealing process. The cathode after surface modification exhibits both enhanced cyclability and improved rate capability compared with the pristine one without coating. The carbon coating process causes a phase transformation from Li_2MnO_3-like domain to cubic-spinel domain with $Fd\bar{3}m$ symmetry at surface regions of particles. As a consequence, the valence state of Mn on the surface varies accordingly. Such

transformed surface spinels as well as the wrapped carbon layers as a result of this coating strategy are believed to be responsible for the enhanced electrochemical performance.

KEYWORDS:

Li-rich layered cathode, carbon coating, phase transformation, Li-ion batteries.

INTRODUCTION

Lithium-rich manganese-based layer-structured cathodes, which could be recognized as either $Li(Li_{1-x-y}Mn_xM_y)O_2$ or $xLi_2MnO_3 \cdot (1-x)LiMO_2$ (M refers to commonly-used transition metals such as Ni and Co), have been attracted extensive interests in a recent years.[1-5] The unique feature of this type of material is its high reversible capacities close to 270 $mAh \cdot g^{-1}$,[4] whereas the traditional layered $Li_{1-x}CoO_2$ is capable of maintaining structural stability only when a half of Li is deintercalated ($x < 0.5$). The integrated Li_2MnO_3 phase can electrochemically be activated with Li extraction accompanied with oxygen release when the potential difference between cathode and anode is higher than 4.5V vs. Li/Li^+ in a first charge process.[6-8] In the following discharge process, the resultant defective MnO_2 structure which has both Li and O vacancies after first charge can adopt the reinsertion of Li where Mn is reduced from tetravalent to trivalent.[1, 9] The ability of one or more Li per unit extraction/reinsertion without obvious collapse from structural instability compared to $Li_{1-x}CoO_2$ is the key for achieving high reversible capacity.

Although the high capacity is very attractive, this family of cathode materials still suffers from several drawbacks: poor cyclability and rate capability, and reducing output voltage during cycling. These drawbacks are believed to be partially associated with the sensitivity of particle surfaces according to recent discoveries on these materials. Gu etc.[10] found that in $Li(Li_{0.2}Ni_{0.2}Mn_{0.6})O_2$ system, Ni prefers to segregate at the surface facets of synthesized particles and the particle facets tend to terminate at transition metal (TM) layers, while the Li fast diffusion channels in these layers are almost perpendicular to the channels inside. In fact, both of the phenomena nearby surface regions could induce high diffusion barrier against Li transportation, leading to poor rate capability. Concerning cyclability, the dissolution of TM ions

in high potential ranges from layered structure is always recognized as a main reason to capacity fade, as suggested by Amine[11] and Song.[12] While another surface initiated effect related to the capacity fade is a phase transformation caused by migration of TM ions, which is driven by thermodynamic instability of Li and O vacancies.[5, 8, 13] Because of the above reasons, such particle surfaces are easily experienced to internal stress leading to local non-crystallization and further micro-cracks on surfaces during cycling.[14]

To address the issues associated to the sensitivity of the particles' surfaces, various methodologies have been used for surface modifications through various coatings of Li–Ni–PO_4,[15] $AlPO_4$,[16] Al[17] and RuO_2[18] as the conductive surface layers to enhance the rate capability. On the other hand, Al_2O_3,[19] ZnO coating layers[20] and surface nitridation[21] were also applied to improve the cycle performance. Besides these traditional protection or conductivity effects resulted from coating layers, AlF_3[22] and MnO_2[23] were also found to contribute to surface spinel formation after corresponding surface modifications. Such surface spinels initiated from original Li_2MnO_3-like domains were reasonably believed to be able to improve both cyclability and rate performance. As a matter of fact, similar improvements due to surface spinels were also observed in $(NH_4)_2SO_4$,[24] graphene[25] and carbon black[26] treated Li-rich layered systems. Nevertheless, due to reduction concerns of carbon coating, only a few of works were reported on the effects of carbon coating on such Li-rich layered systems,[27] although carbon coating is always regarded as the most effective way for enhancement in olivine systems. Therefore, in this work we intend to develop a facile way to achieve carbon coating layers on $Li(Li_{0.2}Mn_{0.54}Ni_{0.13}Co_{0.13})O_2$ particles to improve electrochemical performance without largely change chemical composition of the layered compounds.

EXPERIMENTAL SECTION

Preparation of carbon coated $Li(Li_{0.2}Mn_{0.54}Ni_{0.13}Co_{0.13})O_2$

The pristine Li-rich compound $Li(Li_{0.2}Mn_{0.54}Ni_{0.13}Co_{0.13})O_2$ (LLNCM) was synthesized by a sol-gel method assisted with a spray-drying machine. (YC-015, Shanghai Politech Instrument & Equipment Co. Ltd). The detailed procedures can be found elsewhere,[25] whereas the carbon precursor was prepared based on Fang's work.[28, 29] In a typical synthesis, 0.6 g phenol, 15 ml NaOH aqueous solution (0.1 M) and 2.8 ml formalin solution were mixed and stirred at 70 ^oC for 30 min. Then, 15 ml deionized water containing triblock Pluronic F127 (1.28 g) was added. 2 h later, 50 ml deionized water was added followed by reaction for 20h. The mixture was diluted 4 times before obtaining the pink solution. 300 mg LLNCM and 25 mL pink solution were mixed together by stirring for 1 h. To obtain the carbon coated LLNCM, the mixture was transferred into an autoclave then heating at 130°C for 3 h or 15 h, which are assigned to be C-3 or C-15. After that, the obtained powders were post annealed at 350 °C for 2 h in air with both heating and cooling rates at 5 $°C \cdot min^{-1}$. The corresponding products after post annealing were respectively named as C-3-H and C-15-H.

Structure and morphology characterizations

Crystal structures of all powders were characterized by a powder X-ray diffraction machine (Shimadzu XRD-6000 Cu-Kα radiation, λ = 1.5418 Å). Diffraction data were collected at a scan rate of 0.5^o min^{-1}. Powder morphologies were investigated using a scanning electron microscope (Fe-SEM) (S-4300 Shimadzu, 15kV). A high-resolution transmission electron microscope (HRTEM) (JEOL 2200FS, operating at 200 kV) was employed to reveal the detailed lattice information before and after annealing process. Another scanning transmission electron microscope (JEOL JEM-2010F, operating at 200 kV) coupled with electron dispersive X-ray spectroscopy (EDX) mapping was applied for elemental identification after coating process. The

variations in valence states of transitions metals before and after surface treatment were investigated by X-ray photoelectron spectroscopy (XPS) (Kratos AXIS Ultra DLD, Kratos Analytical Ltd) with a monochromatized Al Kα X-ray source (1486.6 eV photons) at a constant dwelling time of 100 ms. The binding energy was ranged from -5 to 1100 eV. Thermogravimetric analysis (TGA) was applied on C-3 and C-15 samples to reveal the carbon content in air at a heating rate of 5 °C·min^{-1} from room temperature to 800 °C using DTG-60H Shimadzu.

Electrochemical characterizations

Electrochemical behaviors of the pristine and modified samples were tested using CR-2016 type of coin cells. To prepare the coin cells, the electrode slurries were prepared by mixing active cathode materials, carbon black (Super P) and polyvinylidene fluoride (PVDF) in the weight ratio of 80 : 10 : 10 within n-methyl-2-pyrrolidone (NMP) solution stirring for overnight. The slurries were coated on an aluminum foil followed by overnight drying at 120°C. The dried electrodes were punched into pieces of 10 mm diameters with a typical loading of 2 – 3 mg. Half cells were assembled in an argon-filled glove box. Li foil was used as count and reference electrode, two pieces of membrane (Celgard 2500) were adapted separator, and electrolyte in the form of 1M $LiPF_6$ in EC : DEC = 1 : 1 organic solutions was used as the electrolyte. All cycling tests were performed in the potential window of 2.0 – 4.8 V vs. Li/Li$^+$ as 1 C refers to 250 mA·g^{-1}. Plots of dQ/dV vs. voltage were obtained based on the testing data of charge/discharge cycling.

RESULTS AND DISCUSSION

Fig. 1 compares X-ray diffraction spectra of the pristine and the surface modified $Li(Li_{0.2}Mn_{0.54}Ni_{0.13}Co_{0.13})O_2$ powders. All the strong peaks in the patterns could be easily

indexed to a rhombohedral layered phase (subscript of R) with $R\bar{3}m$ space group. Besides these signal reflection peaks, several weak peaks in the range of 20 - 23° are consistent with a super-ordering structure among Li and transition metals (Mn, Ni and Co) in the transition metal layers of Li_2MnO_3-like monoclinic phase (subscript of M).[4] Apparently, no impurity phase could be observed either in carbon coated samples (C-3 and C-15) or post annealed ones (C-3-H and C-15-H). However, the intensity of the super-ordering peaks $(020)_M$ and $(110)_M$ obviously decreases after carbon coating and post annealing, suggesting that the modification process may affect the local ordering of Li_2MnO_3-like phases in crystal lattice in addition to the influence of carbon coating itself. Furthermore, the $(003)_R/(001)_M$ and $(101)_R/(-201)_M$ peaks become broader and shift to higher degrees in the modified samples compared with the peaks in the pristine one. A fitting of C-3-H and C-15-H spectra using Rietveld refinement was successful based on an assumption of Li_2MnO_3 and $LiNi_{1/3}Co_{1/3}Mn_{1/3}O_2$ composite structure, implying only lattice shrink in c - direction after modification rather than new phase formation, which is consistent with the trend observed from acid-treated Li-rich layered cathodes.[30] The hump related to spinel-like ordering phase located at lower 36.9°, as labeled by diamond could be identified in selective XRD patterns in Fig. 1.[22] Based on the above observations, it is likely that the surface coating of carbon leads to a phase transformation from layer-ordering phase to spinel-like phase.

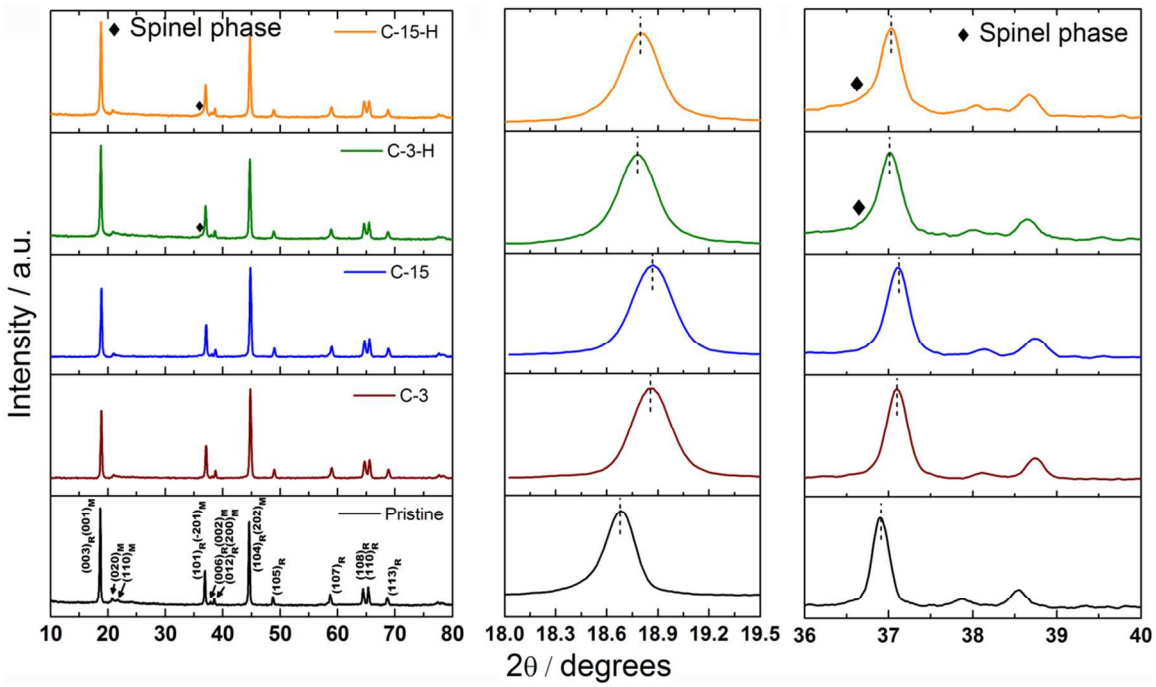

Figure 1. Powder XRD patterns of the pristine, carbon coated (C-3, C-15) and post annealed (C-3-H, C-15-H) LLNCM samples.

Fig. 2 compares morphologies of the pristine, carbon coated (C-3, C-15) and post annealed (C-3-H, C-15-H) particle. The distribution of particle size of about 100 to 200 nm with facets could be observed in the pristine sample, while the particles tend to aggregate and grow in size without clear facet after coating process, as seen in both C-3 and C-15 samples. The increase in particle size is caused by hydrothermal reaction, and might also be associated with carbon coatings which interconnect small crystals. A thin carbon layer about 3 nm was evenly coated on the particles from TEM observation (Fig. 3) whereas parts of carbon were accumulated to form spheres. Elemental mappings of C-3 particle reveal uniform distribution of C, Mn, Ni and Co (Fig. 4) after carbon coating. Similarly but not equally, with the increase in duration time of reaction from 3 to 15 h, more carbon layers in C-15 sample tend to grow into carbon spheres (Fig. 2) which was confirmed in bright field TEM image (Fig. 3). The more transparent spheres

around a LLNCM particle represent the carbon spheres. According to TGA results (Fig. S1), the carbon contents in C-3 and C-15 are approximately 6.3 wt.% and 6.6 wt.%, respectively. A sudden loss of weight from 150 to 300 °C was caused by lose of functional groups on these synthesized carbon. After a post annealing process, the particle morphologies of C-3-H and C-15-H samples barely change but the average particle sizes are apparently reduced compared to those before annealing, as observed in Fig. 2. Moreover, the corresponding TEM images of both C-3-H and C-15-H samples (Fig. S2) exhibit non-uniform transparency in form of nano-domains, compared to dissimilar characters in transparency of pristine sample (Fig. S2). It may imply local disorder or rearrangement of original layered structure as a result of surface treatment, which is highly related to local spinel-like transformation.

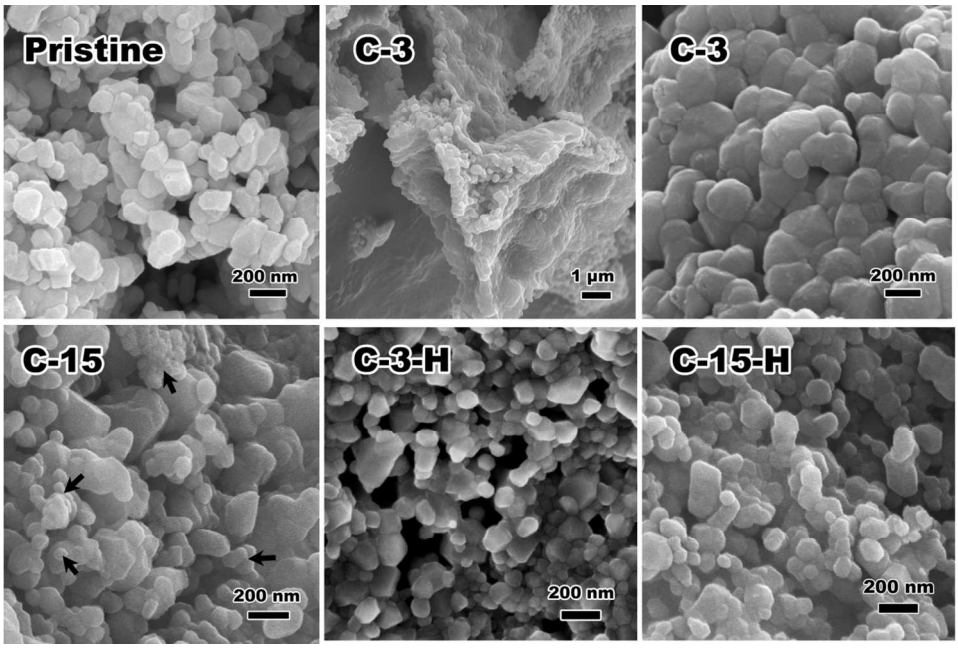

Figure 2. SEM images of the pristine, carbon coated (C-3, C-15) and post annealed (C-3-H, C-15-H) LLNCM particles. Arrows inside indicate the carbon spheres in the C-15 sample.

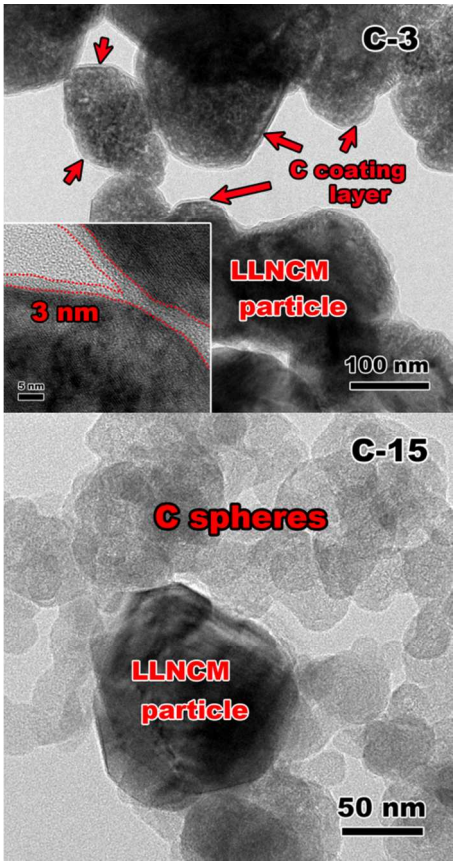

Figure 3. Bright field TEM images of C-3 and C-15 samples where sample of C-3 reveals nano carbon layers of 3 nm thickness on LLNCM particles, while C-15 exhibits carbon spheres around a LLNCM particle instead of coating layers.

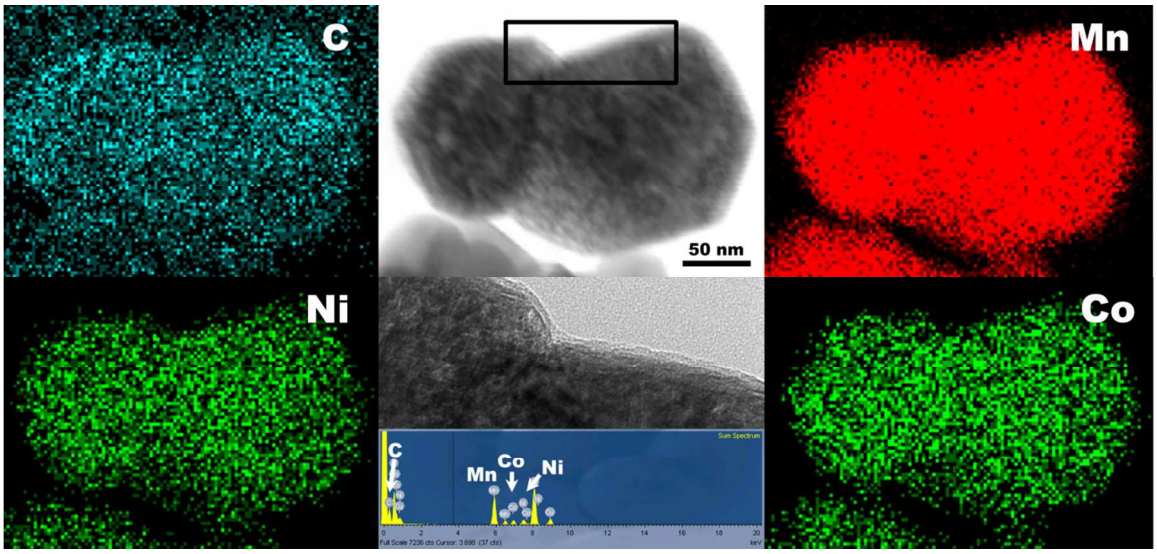

Figure 4. Carbon, nickel, cobalt, and manganese elemental mapping using a STEM on the C-3 sample confirms a uniform distribution of all kinds of elements after coating process.

HRTEM characterization of the C-15-H sample is shown in Fig. 5. Fig. 5 (a) reveals general appearance of the particles with electron diffraction pattern (EDP) and diffraction indexing in Fig. 5 (b) and (c). Two sets of diffraction can be indexed, layered triclinic structure and spinel cubic structure as confirmed. Fig. 5 (d) shows HRTEM on the surface of a particle. Further FFT images for sub areas as shown in Fig. 5 (e) and (f) reveal the spatial relationship between these two phases. Green dash lines in Fig. 5 (d) highlight the layered domains tend to be enclosed by spinel domains which are terminated on the surface of the particle. The zone axis with respect to two phases are $[1\text{-}11]_{layered}$ and $[110]_{spinel}$.

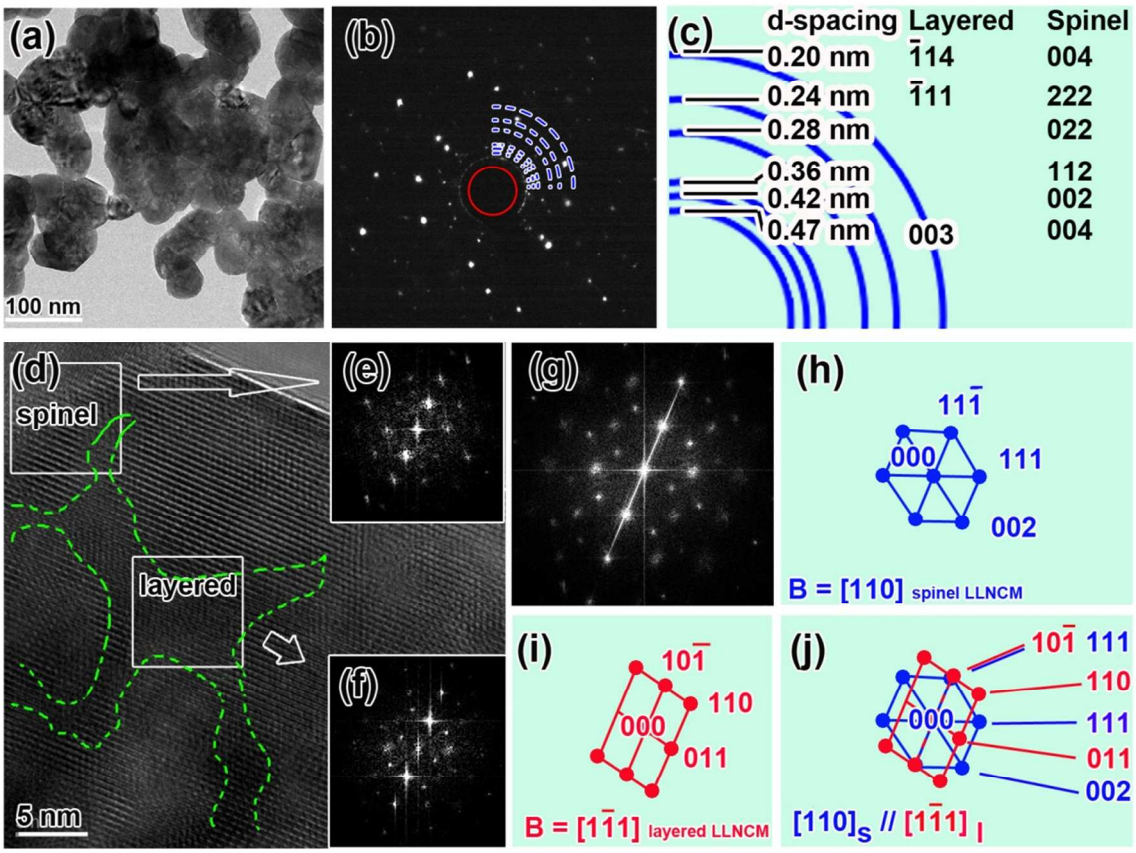

Figure 5. TEM identification of the C-15-H sample: (a) low magnification TEM bright field image of the modified LLNCM particles, (b) electron diffraction pattern (EDP) corresponding to (a), (c) index of the electron diffraction rings of (b), revealing two types of phases i.e., layered triclinic structure and spinel cubic structure, (d) HRTEM image showing surface regions of the particle composed of mixed spinel and layered structures inside, (e) and (f) Fast Fourier Transforms (FFT) to sub areas in (d) with indexes shown in (h) and (i), (g) FFT to (d) with two-phase index shown in (j). The zone axis with respect to two phases are $[1\text{-}11]_{layered}$ and $[110]_{spinel}$. Green dash lines in (d) highlight the layered domain which is enclosed by the spinel domain.

The transformation on the surface regions is believed to be induced during the hydrothermal processing where presence of carbon coating increases the acidity of the hydrothermal solution resulting in ions exchange between H^+ and Li^+ at high pressure. The final annealing may assist phase transformation and aggregation of carbon. On the other hand, the further reduced carbon layers as confirmed by both TGA results (Fig. S1) and TEM image (Fig. S3) could be partially sustained on particle surfaces after heat treatment. Based on the above observations and the synthesis procedure, the mechanisms of carbon coating and transformation on the particles' surfaces in C-3 (C-15) and C-3-H (C-15-H) are schematically illustrated in Fig. 6.

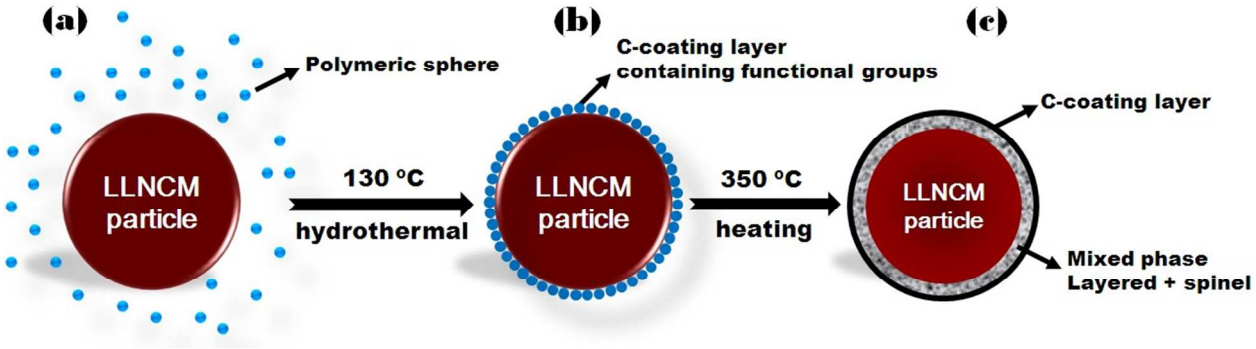

Figure 6. Schematic illustrations of the formation process: (a) mixture of pristine particles and polymeric solution before hydrothermal process, (b) carbon coating with functional groups during hydrothermal processing, and (c) formation of carbon coating and surface transformation.

XPS was applied to investigate the solid-state chemistry of particle surfaces of all the pristine and modified C-3, C-3-H samples. Spectra of C 1s, O 1s, Li 1s, Mn 2p, Ni, 2p and Co 2p orbital are respectively shown in Fig. 7. Curve fittings were performed based on the binding energy of C 1s (C-C sp2 bond) at 284.5 eV. As shown in C 1s spectra, several peaks corresponding to 284.5, 285.5 and 287.6 eV could be recognized as C-C, C-OH and C=O, respectively.[31, 32] The higher intensities of both C-OH and C=O peaks in C-3 sample indicate the presence of functional oxygen groups on the surface carbon layers rather than highly-carbonized layers after coating process. However, these functional groups partially decompose after the post annealing process judged from the drastic decrease in intensities of the C-3-H sample. The similar trend is also observed in the O 1s spectra. A larger amount of functional oxygen groups on particle surface for C-3 sample compared to the amount of pristine one was able to function as the protection layer on particles to mitigate the corrosion effects of electrolyte, and thus enhance the cyclability. In the meantime, these functional oxygen groups could also decrease the surface electrical conductivity of particles. Consequently, these characteristics of functional groups significantly affect the electrochemical performance, and will be shown later. On the other hand, the surface modification has less effects on variations of valence states of both Ni and Co, according to the comparable peaks fitted in Ni 2p and Co 2p spectra. Ni^{2+} (854.6 eV) and Co^{3+} (780.1 eV) dominate in all samples with trace amount of Ni^{3+} (855.9 eV) and Co^{4+} (781.1 eV) at the synthesized state. It is interesting to note that the valence state of Mn substantially varies as a result of carbon coating and post annealing, as seen from both Mn 2p and Mn 3p (close to Li 1s)

spectra. Mn^{4+} with respect to 642.9 eV peak is the majority constitute in the pristine sample, while the majority one switches to Mn^{3+} in both the C-3 and C-3-H samples. The decrease in average valence state of Mn may imply formation of spinel, or at least a change in electronic configuration related to the Mn at surface regions. As also suggested in HRTEM results in Fig. 5, it is likely to deduce that the transformed spinel is $LiMn_2O_4$-like cubic spinel, despite the accurate chemical composition in local structure is hardly detected. However, the statistical feature of the chemical compositions at surface regions of particle could be confirmed by XPS.

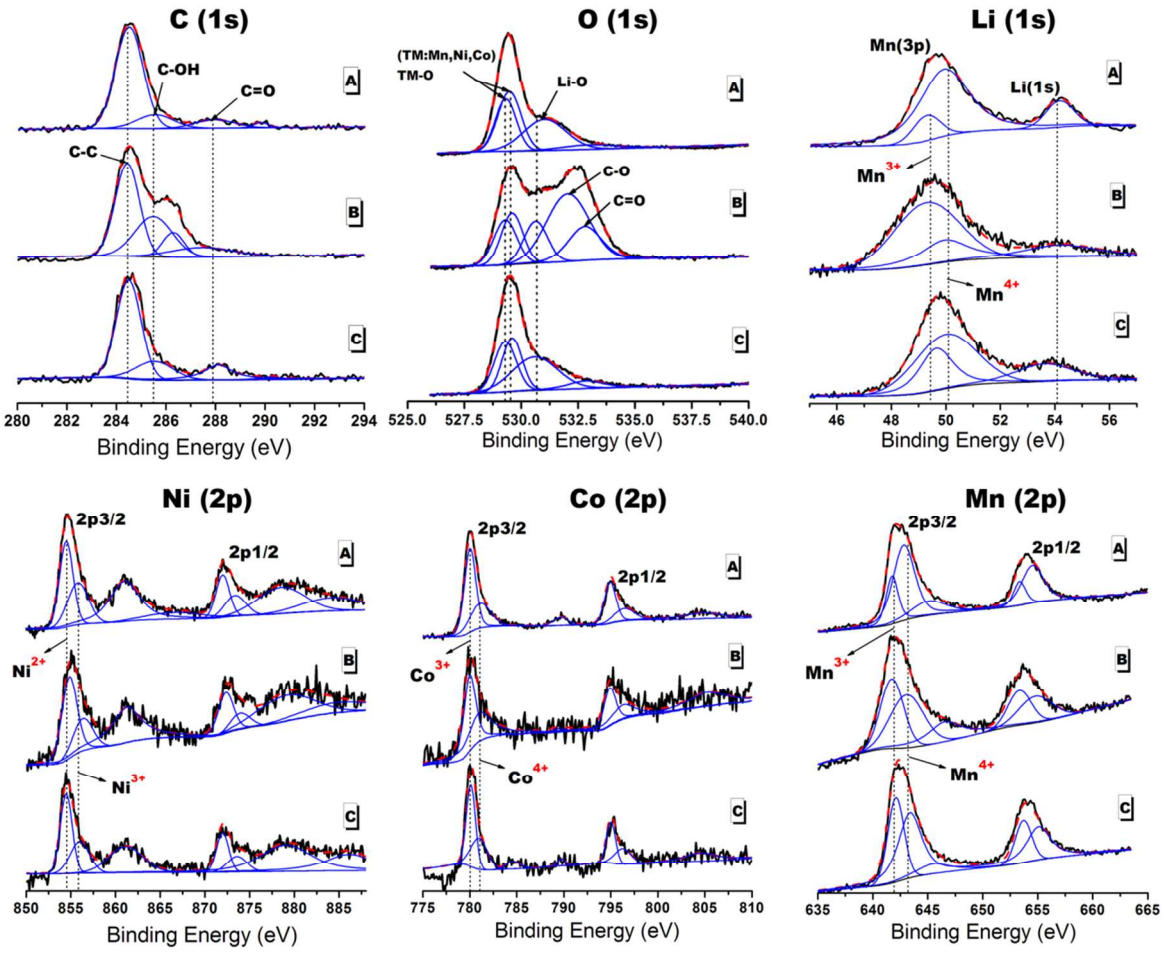

Figure 7. XPS spectra for pristine, C-3 and C-3-H samples as indicated by A, B and C, respectively. Black solid, blue solid and red dash lines represent original graphs, fitted peaks and fitted graphs, respectively.

As shown in Table 1, two important observations are summarized: 1) compositional ratio of Li relative to a sum of TM ions reduces from 1.04 of the pristine to 0.21 of C-3 and to 0.73 of C-3-H, and 2) the relative contents of Ni, Co and Mn also varies. It is important to note that although the above data imply the spinel formation in C-3 sample, a subsequent heat treatment is still necessary to complete such transformation according to distinct electrochemical behaviors in a following section.

Table 1. Surface chemical compositions of the pristine, C-3 and C-3-H samples based on the XPS results.

	Li	Transition metals				O
		Mn	Ni	Co	Total	
Pristine	1.02	0.54	0.22	0.22	0.98	2.8
C-3	0.35	0.91	0.45	0.30	1.65	5.9
C-3-H	0.84	0.84	0.18	0.13	1.15	2.6

Table 2. First charge/discharge capacities and corresponding coulombic efficiency of pristine, C-3, C-15, C-3-H and C-15-H cathodes cycled in a voltage window of 2.0 - 4.8 V at 50mA·g^{-1}.

	Charge capacity (mAh·g^{-1})	Discharge capacity (mAh·g^{-1})	First coulombic efficiency (%)
Pristine	300	253	84.3
C-3	188	116	61.7
C-15	199	142	71.4
C-3-H	272	263	96.7
C-15-H	273	264	96.4

Fig. 8 compares the first cycle charge/discharge curves at a current density of 50 $mA \cdot g^{-1}$ and respective dQ/dV plots of all the samples. The charge/discharge capacities as well as the coulombic efficiencies are tabulated in Table 2. The pristine LLNCM delivers a charge capacity of 300 $mAh \cdot g^{-1}$ and discharge capacity of 253 $mAh \cdot g^{-1}$ with 84 % efficiency, while these values drastically reduce for C-3 and C-15 samples. It is noted that the coated layers of carbon or spheres are of poor electronic conductivity due to their poor carbonization feature, as supported by the presence of functional oxygen groups in XPS C 1s and O 1s results. However, the charge capacities decrease whereas both discharge capacities and coulombic efficiencies increase for C-3-H and C-15-H samples, i.e. 263$mAh \cdot g^{-1}$ with 96.7 % and 264 $mAh \cdot g^{-1}$ with 96.4 %, respectively. These improvements in discharge capacity and initial coulombic efficiency after post annealing could be ascribed to two reasons, formation of spinel by consuming the amount of Li_2MnO_3-like component which is confirmed by reduced 4.5 V charge plateau but elongated 2.7 V discharge plateau, and the better carbonized layers or spheres as a result of post annealing as also supported of XPS results in Fig. 7. Although the pristine LLNCM exhibits a typical deintercalation/intercalation profiles of Li rich layered structure,[2] the typical electrochemical profile has been apparently changed after modification (samples C-3, C-15, C-3-H and C-15-H). The dQ/dV plot of the pristine sample first shows an oxidation of Ni^{2+} and Co^{3+} to higher states related to 4.1 V peak (O_1), followed by a redox-like peak at about 4.6 V which is commonly recognized due to oxygen release. Both of the two peaks clearly shift to higher potentials after coating (C-3, C-15) due to polarization effects from coating layers, but shift back to the comparable positions of the pristine one after the further heating process (C-3-H, C-15-H). In a typical discharge process of the pristine sample, three reduction peaks noted as R_1, R_2 and R_3 were observed. The origin of R_1 is still unclear at present,[33] while R_2 and R_3 are believed to be

associated with Ni^{4+}/Ni^{2+} in addition to Co^{4+}/Co^{3+} redox couples in a layered structure and Mn^{4+}/Mn^{3+} redox in a layered structure, respectively. The only peaks appeared in C-3-H and C-15-H samples, are R_4 and R_5 attributed to the Mn^{4+}/Mn^{3+} redox in a layered-spinel-mixed complex structure and in a surface-formed spinel structure.[34] It is worth pointing out that 1) R_3 contributions in C-3 and C-15 samples significantly reduce compared to the pristine one, suggesting a less activation of Li_2MnO_3-like component which is responsible for reduced discharge capacities, and 2) the existence of only R_4 and R_5 peaks confirms phase transformation after heating process, which not only took place at surface regions but also possibly initiated in bulk regions because of the significant contributions to the capacity. Although XRD and XPS results imply the possible spinel formation in the coated samples C-3 and C-15, the disappearance of R_4 and R_5 peaks still argue that the leaching of Li incorporated with rearrangement of electronic configuration related to Mn occurred, but the local structure sustained to be in the form of layered before the subsequent heating process.

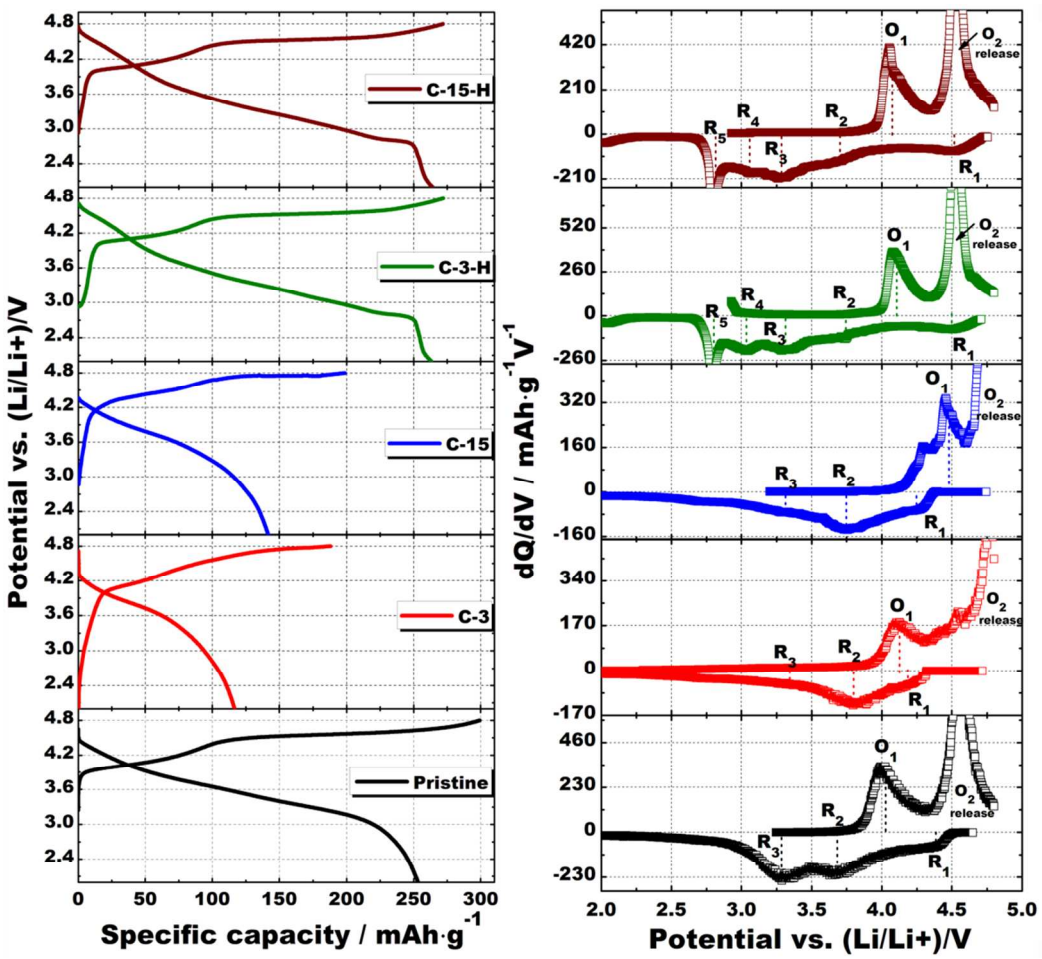

Figure 8. First charge/discharge curves with corresponding dQ/dV plots of the pristine, C-3, C-15, C-3-H and C-15-H cathodes tested at a current density 50 $mA \cdot g^{-1}$, 2.0 - 4.8 V at room temperature.

Fig. 9 shows the cycle performance and rate capability of all the samples. At 0.2 C (Fig. 9(a)), the pristine sample is able to provide 112 $mAh \cdot g^{-1}$ discharge capacity after 100 cycles with 44 % capacity retention, whereas continuous increase in capacities for both C-3 and C-15 samples were observed in the first 8 charge/discharge cycles and 92 % for C-3 and 91 % for C-15 can be obtained. The increase in capacity during charge/discharge upon first 8 cycles is due to continuous activation of Li_2MnO_3 component. As discussed in previous XPS section, the

apparent functional oxygen groups in surface carbon layers may slow down the kinetics of the related activation of Li_2MnO_3. However, it could be further electrochemically reduced to more conductive carbon layers by gradual formation of Li_2O during Li intercalation and deintercalation.[35, 36] The further reduced carbon layers not only facilitate the activation of Li_2MnO_3, but also act as protection layers to avoid thick formation of SEI layers and dissolution of transition metals due to HF attacking.[37-39] In fact, after the initial activation, C-3 and C-15 materials are capable of delivering the capacities as high as 42 and 54 $mAh \cdot g^{-1}$, respectively, at a high rate of 20 C compared with only 13 $mAh \cdot g^{-1}$ for the pristine as shown in Fig. 9(b). On the other hand, the post annealed samples C-3-H and C-15-H possess not only similar initial capacities compared to the pristine one, but also the enhanced ability of capacity retention, i.e. 70 % and 68 %, respectively. It suggests that the sustained carbon layers at particle surfaces after post annealing are still able to function as the protection layers. Furthermore, more than 100 $mAh \cdot g^{-1}$ capacity could be achieved at 10 C from both samples, which might be ascribed to increased extrinsic conductivity of carbon coating as well as the transformed surface spinels providing fast diffusion channels of Li.[40, 41] Meanwhile, it is very important to note that the surface spinels may not be associated with the improved cyceability. On the contrary, it may even negatively contribute to the cyclability since spinel is an unstable phase when exposed to electrolyte (Mn^{2+} dissolution). To better understand the structural evolution process upon cycling, Fig. S4 compares the charge/discharge and dQ/dV curves at various cycling stages of all the samples. As widely accepted, the family of Li-rich layered cathodes is inevitable to be involved with a phase transformation to spinel ordered structure during deintercaltion/intercalation of Li.[12, 13, 42] The pristine material underwent phase transformation in the first 100 cycles. All the other cathodes after surface modification exhibit similar behaviors,

indicating that neither surface coating of carbon nor subsequent heat treatment could contribute to suppress this structural evolution process, as also supported by arrows in dQ/dV plots.

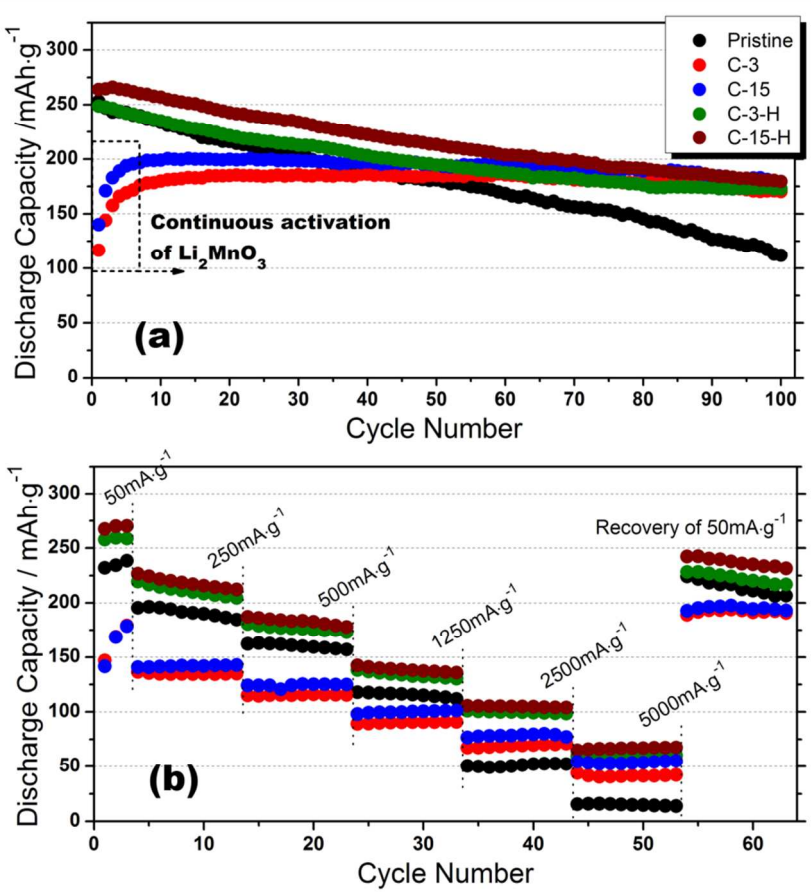

Figure 9. Cycle performance and rate capability of pristine, C-3, C-15, C-3-H and C-15-H cathodes at different testing conditions: (a) 0.2 C, (b) at incremental C rates of 0.2, 1, 2, 5, 10 and 20 C (same current densities for charge/discharge), where 1 C stands for 250 $mAh \cdot g^{-1}$.

CONCLUSIONS

A carbon coating on $Li(Li_{0.2}Mn_{0.54}Ni_{0.13}Co_{0.13})O_2$ has been realized by a hydrothermal approach. The carbon coated $Li(Li_{0.2}Mn_{0.54}Ni_{0.13}Co_{0.13})O_2$ cathode material exhibits enhanced cyclability with discharge capacity 182 $mAh \cdot g^{-1}$ corresponding to 92 % capacity retention after 100 cycles at 0.2 C. After a post annealing of the carbon coated material, increased conductivity of the

carbon layers lead to the enhanced rate capability as well as acceptable cycle performance, i.e. 100 $mAh \cdot g^{-1}$ at 10 C rate and 70 % capacity retention compared with 50 $mAh \cdot g^{-1}$ and 44 % for the pristine material. XRD, HRTEM, XPS and electrochemical testing confirm the formation of spinel domains initiated from Li_2MnO_3-like component, accompanied with variation of valence state of Mn after this surface modification. The spinel benefits in fast diffusion of Li^+ at surface regions and thus the rate capability. However, it may negatively affect cyclability as well. Most importantly, this work provides convincing evidences to support a prospective that the surface characters of the Li-rich layered cathodes are quite sensitive to impact electrochemical performance, not only cyclability but also rate capability.

ACKNOWLEDGEMENT

This work was supported by National Research Foundation, Singapore. The authors are grateful to TIMCAL Ltd. for providing Super PTM conductive carbon black. The authors also acknowledge grant R265-000-426-731/112, Dr. Hongwei Liu for assistance of HRTEM characterizations.

REFERENCES

1. Z. H. Lu, D. D. MacNeil and J. R. Dahn, *Electrochemical and Solid State Letters*, 2001, **4**, A191-A194.
2. B. H. Song, M. O. Lai and L. Lu, *Electrochimica Acta*, 2012, **80**, 187-195.
3. M. M. Thackeray, C. S. Johnson, J. T. Vaughey, N. Li and S. A. Hackney, *Journal of Materials Chemistry*, 2005, **15**, 2257-2267.
4. M. M. Thackeray, S. H. Kang, C. S. Johnson, J. T. Vaughey, R. Benedek and S. A. Hackney, *Journal of Materials Chemistry*, 2007, **17**, 3112-3125.
5. B. Xu, C. R. Fell, M. F. Chi and Y. S. Meng, *Energy & Environmental Science*, 2011, **4**, 2223-2233.
6. A. R. Armstrong, M. Holzapfel, P. Novak, C. S. Johnson, S. H. Kang, M. M. Thackeray and P. G. Bruce, *Journal of the American Chemical Society*, 2006, **128**, 8694-8698.
7. J. Hong, H. D. Lim, M. Lee, S. W. Kim, H. Kim, S. T. Oh, G. C. Chung and K. Kang, *Chemistry of Materials*, 2012, **24**, 2692-2697.
8. N. Yabuuchi, K. Yoshii, S. T. Myung, I. Nakai and S. Komaba, *Journal of the American Chemical Society*, 2011, **133**, 4404-4419.
9. A. Ito, Y. Sato, T. Sanada, M. Hatano, H. Horie and Y. Ohsawa, *Journal of Power Sources*, 2011, **196**, 6828-6834.
10. M. Gu, I. Belharouak, A. Genc, Z. G. Wang, D. P. Wang, K. Amine, F. Gao, G. W. Zhou, S. Thevuthasan, D. R. Baer, J. G. Zhang, N. D. Browning, J. Liu and C. M. Wang, *Nano Letters*, 2012, **12**, 5186-5191.
11. K. Amine, Z. H. Chen, Z. Zhang, J. Liu, W. Q. Lu, Y. Qin, J. Lu, L. Curtis and Y. K. Sun, *Journal of Materials Chemistry*, 2011, **21**, 17754-17759.
12. B. H. Song, Z. W. Liu, M. O. Lai and L. Lu, *Physical Chemistry Chemical Physics*, 2012, **14**, 12875-12883.
13. M. Gu, I. Belharouak, J. M. Zheng, H. M. Wu, J. Xiao, A. Genc, K. Amine, S. Thevuthasan, D. R. Baer, J. G. Zhang, N. D. Browning, J. Liu and C. M. Wang, *Acs Nano*, 2013, **7**, 760-767.
14. A. Ito, D. C. Li, Y. Sato, M. Arao, M. Watanabe, M. Hatano, H. Horie and Y. Ohsawa, *Journal of Power Sources*, 2010, **195**, 567-573.
15. S. H. Kang and M. M. Thackeray, *Electrochemistry Communications*, 2009, **11**, 748-751.
16. Y. Wu, A. V. Murugan and A. Manthiram, *Journal of the Electrochemical Society*, 2008, **155**, A635-A641.
17. J. Liu, B. Reeja-Jayan and A. Manthiram, *Journal of Physical Chemistry C*, 2010, **114**, 9528-9533.
18. J. Liu and A. Manthiram, *Journal of Materials Chemistry*, 2010, **20**, 3961-3967.
19. Y. S. Jung, A. S. Cavanagh, Y. F. Yan, S. M. George and A. Manthiram, *Journal of the Electrochemical Society*, 2011, **158**, A1298-A1302.
20. G. Singh, R. Thomas, A. Kumar, R. S. Katiyar and A. Manivannan, *Journal of the Electrochemical Society*, 2012, **159**, A470-A478.
21. H. Z. Zhang, Q. Q. Qiao, G. R. Li, S. H. Ye and X. P. Gao, *Journal of Materials Chemistry*, 2012, **22**, 13104-13109.
22. Y. K. Sun, M. J. Lee, C. S. Yoon, J. Hassoun, K. Amine and B. Scrosati, *Advanced Materials*, 2012, **24**, 1192-1196.

23. F. Wu, N. Li, Y. F. Su, H. Q. Lu, L. J. Zhang, R. An, Z. Wang, L. Y. Bao and S. Chen, *Journal of Materials Chemistry*, 2012, **22**, 1489-1497.
24. D. Y. W. Yu, K. Yanagida and H. Nakamura, *Journal of the Electrochemical Society*, 2010, **157**, A1177-A1182.
25. B. H. Song, M. O. Lai, Z. W. Liu, H. W. Liu and L. Lu, *Journal of Materials Chemistry A*, 2013, **DOI: 10.1039/c3ta11580a**.
26. B. H. Song, H. W. Liu, Z. W. Liu, P. F. Xiao, M. O. Lai and L. Lu, *Scientific Reports*, 2013, **3**.
27. J. Liu, Q. Y. Wang, B. Reeja-Jayan and A. Manthiram, *Electrochemistry Communications*, 2010, **12**, 750-753.
28. Y. Fang, D. Gu, Y. Zou, Z. X. Wu, F. Y. Li, R. C. Che, Y. H. Deng, B. Tu and D. Y. Zhao, *Angewandte Chemie-International Edition*, 2010, **49**, 7987-7991.
29. Y. Chen, B. H. Song, M. Li, L. Lu and J. M. Xue, *Advanced Functional Materials*, 2014, **24**, 319-326.
30. S. H. Kang, C. S. Johnson, J. T. Vaughey, K. Amine and M. M. Thackeray, *Journal of the Electrochemical Society*, 2006, **153**, A1186-A1192.
31. K. Parvez, S. B. Yang, Y. Hernandez, A. Winter, A. Turchanin, X. L. Feng and K. Mullen, *Acs Nano*, 2012, **6**, 9541-9550.
32. L. Roldan, I. Santos, S. Armenise, J. M. Fraile and E. Garcia-Bordeje, *Carbon*, 2012, **50**, 1363-1372.
33. H. J. Yu, H. J. Kim, Y. R. Wang, P. He, D. Asakura, Y. Nakamura and H. S. Zhou, *Physical Chemistry Chemical Physics*, 2012, **14**, 6584-6595.
34. J. R. Croy, D. Kim, M. Balasubramanian, K. Gallagher, S. H. Kang and M. M. Thackeray, *Journal of the Electrochemical Society*, 2012, **159**, A781-A790.
35. Y. Chen, B. H. Song, X. S. Tang, L. Lu and J. M. Xue, *Journal of Materials Chemistry*, 2012, **22**, 17656-17662.
36. D. Y. Pan, S. Wang, B. Zhao, M. H. Wu, H. J. Zhang, Y. Wang and Z. Jiao, *Chemistry of Materials*, 2009, **21**, 3136-3142.
37. J. F. Ni, L. J. Gao and L. Lu, *Journal of Power Sources*, 2013, **221**, 35-41.
38. K. Edstrom, T. Gustafsson and J. O. Thomas, *Electrochimica Acta*, 2004, **50**, 397-403.
39. S. J. Shi, J. P. Tu, Y. J. Mai, Y. Q. Zhang, C. D. Gu and X. L. Wang, *Electrochimica Acta*, 2012, **63**, 112-117.
40. M. Park, X. C. Zhang, M. D. Chung, G. B. Less and A. M. Sastry, *Journal of Power Sources*, 2010, **195**, 7904-7929.
41. J. Molenda and J. Marzec, *Functional Materials Letters*, 2009, **2**, 1-7.
42. D. Mohanty, S. Kalnaus, R. A. Meisner, K. J. Rhodes, J. L. Li, E. A. Payzant, D. L. Wood and C. Daniel, *Journal of Power Sources*, 2013, **229**, 239-248.

Supporting Information

Additional information includes characterizations by TGA and TEM of carbon-coated samples.

Corresponding Author

* Corresponding author e-mail: luli@nus.edu.sg

Present Address

† Department of Engineering Science, University of Oxford, Parks Road, Oxford OX1 3PJ, UK.